



1 **A Statistical Method for Generating Temporally Downscaled Geochemical**  
2 **Tracers in Precipitation**

3  
4 Catherine E. Finkenbiner<sup>1</sup>, Stephen P. Good<sup>1</sup>, Scott T. Allen<sup>2</sup>, Richard P. Fiorella<sup>3</sup>, Gabriel J.  
5 Bowen<sup>3</sup>

6 <sup>1</sup>*Department of Biological and Ecological Engineering, Oregon State University, Corvallis, OR*

7 <sup>2</sup>*Department of Natural Resources and Environmental Science, University of Nevada, Reno, NV*

8 <sup>3</sup>*Department of Geology and Geophysics, University of Utah, Salt Lake City, UT*

9  
10 *Corresponding Author: Catherine Finkenbiner, c.finkenbiner@gmail.com*

**Early Online Release:** This preliminary version has been accepted for publication in *Journal of Hydrometeorology*, may be fully cited, and has been assigned DOI 10.1175/JHM-D-20-0142.1. The final typeset copyedited article will replace the EOR at the above DOI when it is published.

## ABSTRACT

11  
12 Sampling intervals of precipitation geochemistry measurements are often coarser than those  
13 required by fine-scale hydrometeorological models. This study presents a statistical method to  
14 temporally downscale geochemical tracer signals in precipitation so that they can be used in high-  
15 resolution, tracer-enabled applications. In this method, we separated the deterministic component  
16 of the time series and the remaining daily stochastic component, which was approximated by a  
17 conditional multivariate Gaussian distribution. Specifically, statistics of the stochastic component  
18 could be explained from coarser data using a newly identified power-law decay function, which  
19 relates data aggregation intervals to changes in tracer concentration variance and correlations with  
20 precipitation amounts. These statistics were used within a copula framework to generate synthetic  
21 tracer values from the deterministic and stochastic time series components based on daily  
22 precipitation amounts. The method was evaluated at 27 sites located worldwide using daily  
23 precipitation isotope ratios, which were aggregated in time to provide low resolution testing  
24 datasets with known daily values. At each site, the downscaling method was applied on weekly,  
25 biweekly and monthly aggregated series to yield an ensemble of daily tracer realizations. Daily  
26 tracer concentrations downscaled from a biweekly series had average (+/- standard deviation)  
27 absolute errors of 1.69‰ (1.61‰) for  $\delta^2\text{H}$  and 0.23‰ (0.24‰) for  $\delta^{18}\text{O}$  relative to observations.  
28 The results suggest coarsely sampled precipitation tracers can be accurately downscaled to daily  
29 values. This method may be extended to other geochemical tracers in order to generate downscaled  
30 datasets needed to drive complex, fine-scale models of hydrometeorological processes.

## 31 **1. Introduction**

32 Naturally occurring chemical signatures in precipitation (e.g. Bailey et al. 2018, Bowen et  
33 al. 2019, Gibson et al. 2005, Kendall and McDonnell 2012, Moerman et al. 2013, West et al. 2010,  
34 Wiederhold 2015) are frequently used as hydrometeorological tracers, especially when inferring  
35 transport or chemical transformations through terrestrial, aquatic, and atmospheric environments  
36 (e.g. Abbott et al. 2016, Brooks et al. 2014, Good et al. 2015, Gupta et al. 2020, Kanner et al. 2014,  
37 Remondi et al. 2018). Tracer-enabled modeling allows for process-level inference based not only  
38 on the size of fluxes, but also on the spatial and temporal transport and mixing of the geochemical  
39 signatures associated with the fluxes, thereby facilitating improved understanding and multi-  
40 response model evaluation (Bowen and Good 2015, Krause et al. 2005, McGuire and McDonnell  
41 2006, Sprenger et al. 2019, Turnadge and Smerdon 2014). Researchers have used tracers within  
42 global climate models to evaluate processes that are challenging to observe (e.g. ageostrophic  
43 circulations, convection and turbulence) or are modeled at sub-grid scales and are therefore not  
44 explicitly simulated but parameterized (e.g. Gupta et al. 2020, Orbe et al. 2020, Rosa et al. 2012).  
45 For instance, isotope-enabled general circulation models (GCMs) have explicitly simulated water  
46 isotope ratios within the critical zone on sub-daily time scales (e.g., a version of the Community  
47 Earth System Model (iCESM1); Brady et al. 2019, Nusbaumer et al. 2017, Wong et al. 2017) and  
48 provide outputs which have been evaluated against observational datasets at various scales (e.g.,  
49 Hoffmann et al. 2000, Nusbaumer et al. 2017, Risi et al. 2012, Steen-Larsen et al. 2016, Wong et  
50 al. 2017).

51 In many modeling applications, observed and modeled temporal resolutions are different  
52 and, in these cases, a downscaling method is required in order to use observed datasets within a  
53 model to evaluate processes with dynamic fluctuations over short temporal intervals (Ebtehaj and

54 Fofoula-Georgiou 2013). The temporal resolution at which many geochemical tracers are  
55 collected, a result of analytical or logistical cost or the need to aggregate them in time to achieve  
56 a measurable signal due to low tracer concentrations, contrasts with the time steps typical of many  
57 hydrometeorological models (Rosa et al. 2012, Gupta et al. 2020). Accordingly, a method is  
58 needed to generate higher frequency datasets of precipitation chemistry from low frequency  
59 collections.

60 Statistical downscaling leverages relationships observed in both fine- and coarse-scale  
61 measurements to predict fine-scale variations where only coarse-scale data are available (Ebtehaj  
62 and Fofoula-Georgiou 2013, Goncu and Albek 2016). Extensive work has focused on  
63 downscaling precipitation rate, including through use of temporal neural networks (e.g. Coulibaly  
64 et al. 2005), stochastic methods (e.g. Bordoy and Burlando 2013, D’Onofrio 2013, Poduje and  
65 Haberlandt 2017), and conditional multivariate statistical models (e.g. Yang et al. 2010). However,  
66 past studies have not temporally downscaled precipitation chemistry data, as is warranted for tracer  
67 applications.

68 Precipitation stable isotope ratios ( $\delta^2\text{H}$  and  $\delta^{18}\text{O}$ ) are an ideal test case for developing a  
69 downscaling method that can benefit tracer applications, if the downscaling can preserve multi-  
70 scale statistical properties (Ebtehaj and Fofoula-Georgiou 2013). Not only is such downscaling  
71 in demand, decades of research demonstrate patterns in precipitation isotope ratios that could be  
72 leveraged in downscaling; specifically, precipitation amount often covaries with isotopic  
73 composition, attributable to the interplay of diverse climatological, physiographical, and  
74 meteorological factors in the evaporation, condensation, and transport of atmospheric moisture  
75 (e.g. Aggarwal et al. 2016, Aggarwal et al. 2012, Bowen et al. 2019, Ingraham 1998, Konecky et  
76 al. 2019, Lee and Fung 2008, Moore et al. 2016, Risi et al. 2008, West et al. 2010). This (typically

77 inverse) covariation between precipitation rates and isotope ratios, often referred to as an “amount  
78 effect”, represents partially systematic variations at sub-seasonal, monthly, and event time scales  
79 (Celle-Jeanton et al. 2001, Conroy et al. 2016, Craig 1961, Craig and Gordon 1965, Gat 1996, Lee  
80 and Fung 2008, Moore et al. 2013, Tharammal et al. 2017). If these amount effects share statistical  
81 similarities across various time scales, they could support downscaling methods to predict short-  
82 term fluctuations. Hypothetically, relationships inferred from sporadic or brief datasets could be  
83 used to predict short term variations in precipitation isotopic composition. Those patterns could be  
84 superimposed on the longer timescale seasonal patterns, which tend to follow regional patterns  
85 (Bowen et al. 2019, Dansgaard 1964, Feng et al. 2009, Allen et al. 2019), to potentially generate  
86 realistic, continuous, high-frequency time series of precipitation isotope ratios.

87           In this study, we developed and evaluated a downscaling method that uses the statistical  
88 structure of observed stable isotope time series to downscale and generate stable isotope time series  
89 at finer resolutions. We used daily observations of precipitation amounts and isotope ratios from  
90 27 monitoring stations across the globe. The daily data were artificially aggregated to weekly,  
91 biweekly and monthly scales, using amount-weighted running means to simulate coarser-scale  
92 datasets on which to apply the method. These aggregated time series were evaluated for statistical  
93 trends, specifically characterizing how the time-series means, standard deviations and correlation  
94 structures changed as the temporal sampling interval increased. Then, the statistical downscaling  
95 method was applied on each of the weekly, biweekly and monthly aggregated tracer time series to  
96 generate downscaled tracer values. An ensemble of downscaled realizations was generated at each  
97 site, the statistics of which were compared to those of the original daily observations. Our objective  
98 was to generate downscaled realizations that accurately preserved the observed daily  $\delta^2\text{H}$  and  $\delta^{18}\text{O}$

99 means and standard deviations and the correlation structure between precipitation amount,  $\delta^2\text{H}$ ,  
100 and  $\delta^{18}\text{O}$ , so that these realizations could be suitable for various potential modeling applications.

101

## 102 **2. Data and Methods**

### 103 *a. Site Information and Tracer Datasets*

104 Daily precipitation stable water isotope time series were downloaded from the International  
105 Atomic Energy's (IAEA) Global Network of Isotopes in Precipitation (GNIP) and Water Isotope  
106 System of Data Analysis, Visualization and Electronic Retrieval (WISER) database (IAEA/WMO  
107 2020). Each time series was filtered to ensure precipitation values were greater than zero and had  
108 corresponding  $\delta^2\text{H}$  and  $\delta^{18}\text{O}$  isotope ratios. All time series with greater than one year of  
109 observations were selected, resulting in the 27 datasets used in the subsequent analysis; details  
110 pertaining to each site are included in Table S1 located in the *Supplementary Materials*. A  
111 minimum time series length of one year was chosen because we wanted to account for site-specific  
112 seasonal precipitation patterns in the generated downscaled tracer time series. We acknowledge  
113 seasonality is usually characterized over time scales greater than one year, however for this  
114 analysis we decided on a minimum of one year so the downscaling method could be applied to as  
115 many datasets as possible. In the *Discussion*, the downscaling method's performance was  
116 evaluated against the number of years represented in the time series and the frequency of  
117 collection, i.e. the number of recorded precipitation events divided by the total number of days  
118 represented in the time series. The time series lengths ranged from 1.22 to 15.94 years, with an  
119 average of 5.34 years. The total number of samples in a time series ranged from 33 to 1026, with  
120 an average of ~210. The site with 33 samples (Barasat, Kolkata; Table S1) was sampled over 1.33  
121 years.

122 All hydrogen and oxygen isotope ratios of precipitation were denoted as  $\delta^2\text{H}$  and  $\delta^{18}\text{O}$ ,  
123 defined by

$$125 \quad \delta (\text{‰}) = \frac{R_{\text{sample}} - R_{\text{std}}}{R_{\text{std}}} 1000 \quad \text{Eq. 1}$$

126  
127 where  $\delta$  was the isotope ratio in delta notation,  $R_{\text{sample}}$  was the ratio of concentrations between the  
128 rare and abundant isotopologues, and  $R_{\text{std}}$  was the isotopic ratio standard; for this analysis, that  
129 standard was the Vienna Standard Mean Ocean Water (VSMOW). The site locations and average  
130 stable water isotope observations were represented in Figure 1. The 27 sites have an average mean  
131 (+/- standard deviation) daily observed precipitation of 22.80 (21.38) mm,  $\delta^2\text{H}$  of -37.77 (24.62)  
132 ‰ and  $\delta^{18}\text{O}$  of -6.03 (3.21) ‰. The maximum recorded total daily precipitation ranged from 43.0  
133 to 317.5 mm across sites. At the 27 sites, the observed isotope ratios ranged from -228.0 to 43.35  
134 ‰ for  $\delta^2\text{H}$  and -30.50 to 8.81 ‰ for  $\delta^{18}\text{O}$ . The site list included geographic locations across  
135 different climates and with uniform and seasonally varying precipitation amounts.

136 Isotope ratios are often evaluated relative to the Global Meteoric Water Line (GMWL),  
137 which is defined as  $\delta^2\text{H} = 8\delta^{18}\text{O} + 10 \text{‰}$  (Craig, 1961). Deuterium excess (*d*-excess  
138 (‰) =  $\delta^2\text{H} - 8\delta^{18}\text{O}$ ) measures the deviation of a water sample's composition from the GMWL  
139 (Dansgaard, 1964) and is a useful secondary tracer in that it varies with respect to the evaporation  
140 and mixing history of airmasses (e.g., Benetti et al. 2014, Fröhlich et al. 2002, Pfahl and Sodemann  
141 2014). One can use *d*-excess to understand both the source of precipitation and the evolution of  
142 moisture during transport (Fröhlich et al. 2002, Good et al. 2014). We aimed to preserve a site's  
143 *d*-excess in the downscaled time series because it can be informative for a variety of hydrological  
144 and meteorological applications.

145

146 *b. Constructing Low-resolution Datasets*

147 We aggregated each of the 27 GNIP site's datasets using a moving, precipitation amount-  
148 weighted average (Eq. 2). This provided us with datasets of low-resolution tracer time series on  
149 which to apply the downscaling method to generate downscaled daily estimates to compare with  
150 the observed daily values. The precipitation amount-weighted average was defined as

151

152 
$$\overline{\delta^2 H}_t = \frac{\sum_{i=1}^t P_i \delta^2 H_i}{\sum_{i=1}^t P_i} \text{ and } \overline{\delta^{18} O}_t = \frac{\sum_{i=1}^t P_i \delta^{18} O_i}{\sum_{i=1}^t P_i} \quad \text{Eq. 2}$$

153

154 where  $P$  was total precipitation (mm),  $\delta^2 H$  (‰) and  $\delta^{18} O$  (‰) were the daily observed stable  
155 water isotope tracer values at time  $t$  (days), and  $\overline{\delta^2 H}_t$  (‰) and  $\overline{\delta^{18} O}_t$  (‰) were the  $t$ -day average  
156 tracer value within the specified aggregated temporal interval.  $\overline{\delta^2 H}_t$  and  $\overline{\delta^{18} O}_t$  values populated  
157 a time series at  $t$  level of aggregation. We focused on downscaling time series aggregated at  $t$   
158 values of 7-, 14-, and 28-days (weekly, biweekly, and monthly).

159 Time series statistics were evaluated across a range of temporal intervals. Moerman et al.  
160 (2013) investigated the correlation structure between precipitation amount and  $\delta^{18} O$  at Mulu  
161 Meteo, Sarawak (Table S1) at daily to 12-week (84-days) time scales. Following their approach,  
162 we evaluated trends in the mean ( $\mu$ ), standard deviation ( $\sigma$ ), and Pearson correlation coefficient  
163 ( $\rho$ ) at different temporal intervals to capture the time series response and prediction accuracy. The  
164  $\rho$  measures the linear correlation between two variables and has a value between -1 and 1, where  
165 1 is a total positive linear correlation, 0 is no linear correlation, and -1 is total negative linear  
166 correlation. At the daily scale for the 27 GNIP sites, the average (+/- standard deviation)  $\rho(P, \delta^2 H)$   
167 was -0.18 (+/- 0.18),  $\rho(P, \delta^{18} O)$  was -0.20 (+/- 0.17) and  $\rho(\delta^2 H, \delta^{18} O)$  was 0.96 (+/- 0.03).



168

169 *c. Statistical Precipitation Tracer Downscaling Method*

170 1) REMOVAL OF THE DETERMINISTIC TIME SERIES COMPONENT

171 Each aggregated weekly, biweekly and monthly time series (Eq. 2) was treated as an  
172 example of a low-resolution dataset on which to apply the downscaling method. We considered  
173 each tracer time series to have a deterministic component and a stochastic component. In the first  
174 step, the deterministic component was characterized by the seasonality in the precipitation signal  
175 and was removed from each set of observations. Isotope ratios in precipitation frequently have  
176 been observed to exhibit distinct seasonal signals. These can be approximated as a combination of  
177 sinusoidal functions through Fourier decomposition (Allen et al. 2018, Allen et al. 2019, Dutton  
178 et al. 2005, Feng et al. 2009, Halder et al. 2015, Vachon et al. 2007, Wilkinson and Ivany 2002).  
179 Sinusoidal functions effectively describe the collinear structure and fluctuations in the covariation  
180 of  $\delta^2\text{H}$  and  $\delta^{18}\text{O}$  relative to the GMWL (Figure 1; Allen et al. 2018, Craig 1961, Dansgaard 1964).  
181 The sine curve parameters (amplitude, phase, and offset) are often predictable in space (Allen et  
182 al. 2018, Jasechko et al. 2016) and succinctly represent temporal dynamics because they express  
183 continuous, cyclic time series. Allen et al. (2019) used monthly isotopes in precipitation GNIP  
184 datasets from across the globe to capture patterns in the precipitation isotope seasonality using  
185 sinusoidal functions. When predicting the isotope seasonality, the values of the sine parameters  
186 can be described as functions of climate and geography. Additionally, sine curves are useful when  
187 describing the propagation of cyclic signals, this has been done to infer catchment-scale mixing  
188 processes using the dampening ratio of seasonal isotope amplitudes in streamflow versus  
189 precipitation (Kirchner 2016a, 2016b; also see Clow et al. 2018, von Freyberg et al. 2018, Gallart  
190 et al. 2020, Jacobs et al. 2018, Jasechko et al. 2016, Lutz et al. 2018, Song et al. 2017).

191 We fitted sinusoidal functions to each of the site's daily to 12-week aggregated time series  
192 to describe the deterministic components using a non-linear, least squares fitting routine,  
193 "curve\_fit" in Python's (v3.7.6) SciPy Library (v1.2.1), following the methods from Allen et al.  
194 (2018). We used a time-weighted fit routine (i.e., not amount weighted and each daily sample had  
195 equal weight) to approximate the parameters of the sinusoidal function (Eq. 3) because our ultimate  
196 goal related to predicting daily precipitation variations in isotopic composition, regardless of  
197 whether or not they are associated with larger events. The sine functions were defined with a fixed  
198 period of one year and

199

$$200 \text{ Precipitation } \delta^2H \text{ or } \delta^{18}O(f) = A \sin(2\pi f - \phi) + b, \quad \text{Eq. 3}$$

201

202 where  $f$  was the fractional year and  $b$  was an offset parameter (Allen et al. 2018). All fitted  
203 amplitudes ( $A$ ) and phases ( $\phi$ ) were bounded so the amplitude values were positive and the phase  
204 ranged between  $-\pi$  and  $\pi$ . The presence of large seasonal isotope cycles enables the quantification  
205 of mixing, transport and turnover of water in landscape and/or biota. Amplitude dampening reflects  
206 mixing processes, phase shifts reflect advective travel times and offset differences reflect  
207 proportional contributions of different seasons' precipitation (Kirchner 2016a, 2016b). The  
208 defined sinusoidal functions were subtracted from the daily to 12-week aggregated series, thus  
209 removing the deterministic time series components.

210

## 211 2) GENERATION OF STOCHASTIC TRACER REALIZATIONS

212 Next, the daily statistics of the stochastic hydrogen ( $\delta^2H^*$ ) and oxygen ( $\delta^{18}O^*$ ) isotope  
213 time series were estimated by using the relationship between the observed daily stochastic statistics

214 and the stochastic signal's statistics across a range of aggregation intervals ( $t$ ) multiplied by each  
215 site's specific precipitation frequency ( $\lambda$ ; defined as the number of days with precipitation divided  
216 by the total number of days in a time series). The statistics of the stochastic signal at aggregation  
217 interval  $t$  were denoted with \* as  $\mu_t^*$ ,  $\sigma_t^*$ , and  $\rho_t^*$  and estimates of these at the daily ( $t=1$ ) resolution  
218 were denoted as  $\hat{\mu}_1^*$ ,  $\hat{\sigma}_1^*$ , and  $\hat{\rho}_1^*$ . After removal of the deterministic component, the stochastic  
219 signals had mean isotope values of approximately zero across all ranges of  $t\lambda$  (Figure 2.a,b).  
220 Consequently, we assumed the stochastic signal to behave as a purely random mean zero process  
221 ( $\hat{\mu}_1^* = 0$ ), which was further substantiated using tests for independence, autocorrelation, and  
222 normality on the stochastic signal (refer to *Sections 2.d* and *3.d*).

223         The time series standard deviations were greatest at daily time scales and decreased with  
224 increasing  $t\lambda$  as a power law function (Figure 2.c,d). This decrease resulted from the averaging  
225 and weighting of individual daily tracer concentrations by precipitation amounts over longer  
226 temporal intervals. By the Central Limit Theorem and the Law of Large Numbers, as the sampling  
227 size increases, the sampling distribution converges to a normal distribution where the standard  
228 deviation decreases at a rate of  $1/n^{0.5}$ , where  $n$  is a number of samples. It should be noted, the  
229 results from the Central Limit Theorem and the Law of Large Numbers holds as long as the signal  
230 is purely stochastic and there are no trends or heteroscedasticity in the time series. It was assumed  
231 a similar relationship was held between the daily standard deviation of days with precipitation  
232 tracer values ( $\sigma_1^*$ , ‰) and the series of known  $t$ -day aggregation intervals (days) with their  
233 corresponding standard deviations in time ( $\sigma_t^*$ , ‰).  $t\lambda$  estimated the expected number of  
234 precipitation events in each aggregation level because precipitation does not occur every day (e.g.  
235  $n \approx t\lambda$ ). We expressed this relationship as

236

237  $\sigma_t^* = \frac{\hat{\sigma}_1^*}{(t\lambda)^a},$  Eq. 4

238

239 where  $a$  is a site-specific parameter defining the rate decrease in  $\sigma_t^*$  with increasing  $t$ . We used the  
240 non-linear, least-squares fitting routine, “curve\_fit”, in Python’s (v3.7.6) SciPy Library (v1.2.1) to  
241 estimate the  $a$  and  $\hat{\sigma}_1^*$  parameters in Eq. 4.  $a$  was constrained between 0.2 and 0.5 in order to  
242 bound the curve fitting routine. When  $\hat{\sigma}_1^*$  was compared with  $\sigma_1^*$ ,  $a$  values below 0.2 often  
243 underpredicted  $\hat{\sigma}_1^*$  and above 0.5 often overpredicted  $\hat{\sigma}_1^*$ . The initial value predicted for  $a$  was set  
244 at 0.3, however varying this had negligible influence on the final  $a$  parameter estimates and the  $a$   
245 parameter estimates were not strongly related to observed standard deviation (for  $\delta^2\text{H}^*$  and  $\delta^{18}\text{O}^*$   
246  $R^2 < 0.002$  and p-value  $> 0.75$ ). To estimate the daily standard deviation at a site with a biweekly  
247 ( $t = 14$ ) sampling frequency, first  $\lambda$  must be calculated and the time series can be aggregated to  
248 28-, 42-, 56-, 70-, and 84-day intervals (Eq. 2) for  $2t$  to  $6t$ , giving 6 points to fit Eq. 4. Weekly time  
249 series were aggregated from  $2t$  to  $12t$  (12 points), while monthly time series were aggregated from  
250  $2t$  to  $3t$  (3 points). This quantified the decrease in  $\sigma_t^*$  from the available data resolution out to 12  
251 weeks (84-days), and allows  $a$  and  $\hat{\sigma}_1^*$  to be estimated.

252 The ratio of  $\rho_t^*$  divided by  $\rho_1^*$  across  $\lambda t$  was relatively invariant and centered around one  
253 (Figure 2.e-g). Thus, Pearson correlation coefficients at a  $t$ -day aggregation interval ( $\rho_t^*$ ) were used  
254 to describe the daily correlations ( $\hat{\rho}_1^*$ ) between precipitation amount and the stochastic signal’s  
255  $\delta^2\text{H}^*$  and  $\delta^{18}\text{O}^*$  values.

256 Pseudo-random numbers were generated using a Gaussian copula (Sklar 1959), defined by  
257 the estimated daily statistics,  $\hat{\mu}_1^*$ ’s,  $\hat{\sigma}_1^*$ ’s, and  $\hat{\rho}_1^*$ ’s, and conditioned on the observed daily  
258 precipitation amounts. Other copula families are possible (e.g. Archimedean copula, Gumbel  
259 copula); however, here the Gaussian copula was used because it offered a simple approach for

260 modeling the dependence of multivariate states (Schneider and Ramos 2014). In probability theory  
261 and statistics, the marginal distribution of a subset of a collection of random variables is the  
262 probability distribution of one random variable without any reference to other random variables.  
263 Copula models separate the dependency structure of multiple random variables from their marginal  
264 distributions by mapping each variable through its cumulative distribution functions (CDF) to the  
265 unit interval (i.e. closed interval [0,1]). This captures the dependence between the variables using  
266 a copula or coupling term, allowing a different marginal distribution for each variable while  
267 capturing the multivariate dependencies (Schneider and Ramos 2014, Sklar 1959). Here, a copula  
268 captured the multivariate dependencies between precipitation amount,  $\delta^2H^*$  and  $\delta^{18}O^*$ . Refer to  
269 *Supplemental Material* for further detail on the definition of the Gaussian copula used here. Models  
270 using copula techniques have captured the spatial and temporal patterns of precipitation  
271 characteristics (Kuhn et al. 2007, Gao et al. 2018), temporally downscale precipitation datasets  
272 (Gyasi-Agyei 2011, So et al. 2017), to forecast precipitation events (Bárdossy and Pegram 2009,  
273 Khedun 2014) and across other hydrological disciplines (e.g. temperature and rainfall dynamics  
274 (Cong and Brady 2012, Schölzel and Friederichs 2008), extreme-value stochastic rainfall events  
275 (Kuhn et al. 2007, Laux et al. 2011, Huang et al. 2012), drought distributions from monthly rainfall  
276 (Laux et al. 2009), hydraulic conductivity of aquifer systems (Haslauer et al. 2012), and  
277 groundwater recharge from precipitation events (Jasechko and Taylor 2015).

278 For each observed precipitation amount, values of  $\delta^2H^*$  and  $\delta^{18}O^*$  (a 2-number sample  
279 representing the stochastic signal) were drawn from a multivariate Gaussian distribution using  
280 Python's (v3.7.6) SciPy Library (v1.2.1) with parameters described by  $\hat{\rho}_1^*(P, \delta^2H^*)$ ,  
281  $\hat{\rho}_1^*(P, \delta^{18}O^*)$  and  $\hat{\rho}_1^*(\delta^2H^*, \delta^{18}O^*)$  (refer to Eq. 9 and 10 in the *Supplemental Material*). The  
282 covariates used here were precipitation amount and its isotopic composition, however it should be

283 noted the covariates can change depending on the method's application and data availability. Next,  
284 Gaussian CDF values were calculated for each of the generated series. The resulting uniform  
285 values were then used to resample from the coarse resolution empirical distribution of isotope  
286 ratios for each site, formed by the deseasonalized time series. Each of these values was then  
287 rescaled by  $\hat{\sigma}_1^*/\sigma_t^*$ . The resulting stochastic time series were daily  $\delta^2\text{H}^*$  and  $\delta^{18}\text{O}^*$  values  
288 conditioned on observed precipitation amounts with means of zero, standard deviations of  $\hat{\sigma}_1^*$  and  
289 Pearson correlation coefficients of  $\hat{\rho}_1^*$ .

290

### 291 3) FULL SYNTHETIC TIME SERIES GENERATION

292 The deterministic component, the sinusoidal function from Eq. 3, was added to each  
293 generated stochastic time series. The result was a downscaled tracer time series which captured  
294 site-specific daily precipitation amount effects, seasonal signals and stochastic variability. Finally,  
295 we applied a residual correction on the downscaled synthetic series to preserve the observed  
296 aggregated weighted tracer values. For each synthetic value within each aggregation interval, an  
297 interval-specific, single correction factor was subtracted from the downscaled values so that there  
298 was no difference between that period's downscaled synthetic values aggregated for that interval  
299 and the observed coarse-resolution interval's value. In doing so, the precipitation-weighted values  
300 of the synthetic time series then equaled the known aggregated value. This property is particularly  
301 important as it closes the tracer mass balance. The statistical downscaling method applied to a  
302 dataset with a biweekly sampling frequency was summarized and visualized in *Section (ii)* of the  
303 *Supplemental Material*.

304

305 *d. Evaluation of Precipitation Tracer Downscaling Mythology*

306 The statistical method was iterated over 100 times generating an ensemble of downscaled  
307 isotope time series at each of the 27 GNIP locations. The large number of time series generated  
308 for each ensemble allowed for us to quantify the performance of the downscaling method. Each  
309 ensemble was expected to capture the observed site-specific tracer means and standard deviations  
310 and the correlation coefficients between precipitation amount,  $\delta^2\text{H}$  and  $\delta^{18}\text{O}$ . The statistical  
311 downscaling method was evaluated using multiple techniques, detailed in the subsequent  
312 paragraphs.

313 After removing the deterministic components, the stochastic time series were expected to  
314 have means of approximately zero, a predictable decrease in standard deviation (Eq. 4) and Pearson  
315 correlation coefficients at low temporal resolutions appropriately defining daily covariate  
316 structures. To test this,  $\sigma_1^*$  and  $\rho_1^*$  of the observed datasets were compared to  $\hat{\sigma}_1^*$  and  $\hat{\rho}_1^*$  of  
317 downscaled ensembles using root-mean squared error (RMSE), mean bias error (MBE), and R-  
318 squared ( $R^2$ ). Autocorrelations with lags ranging from 1- to 20-days (Figure 6, refer to *Section 3.c*)  
319 and tests for normality were calculated for the stochastic signal of the observed datasets and  
320 downscaled ensembles.

321 The average of ensemble means ( $\overline{\hat{\mu}_1}$ ) and standard deviations ( $\overline{\hat{\sigma}_1}$ ) for each isotope ratio  
322 and the Pearson correlation coefficients ( $\overline{\hat{\rho}_1}$ ) between precipitation amount and each isotope ratio  
323 were compared to the observed daily statistics.  $R^2$  values were calculated for the downscaled  
324 ensembles and observed daily site statistics. Each site's observed  $d$ -excess was evaluated against  
325 the downscaled ensemble's  $d$ -excess. Lastly, we compared the absolute error between the  
326 downscaled ensemble and observed time series means to various site-specific and time series  
327 characteristics.

328

### 329 3. Results

#### 330 a. Evaluation of Estimated Daily Stochastic Signal Statistics

331 The estimated daily stochastic signal statistics from weekly, biweekly and monthly  
332 aggregation intervals accurately described the observed statistics (Figure 3). The method best  
333 predicted  $\hat{\sigma}_1^*$  when applied to a weekly series, while the worst approximations of  $\hat{\sigma}_1^*$  occurred when  
334 it was applied to a monthly series. We expected the weekly time series to best predict  $\hat{\sigma}_1^*$  because  
335 it better characterizes the change in tracer concentration variance as more values of  $t$  were used to  
336 fit the  $\hat{\sigma}_1^*$  and  $a$  parameters in Eq. 4. For all 27 GNIP sites, the  $\delta^2\text{H}$   $\hat{\sigma}_1^*$  had RMSEs of 2.73 ‰  
337 (MBE = -1.92 ‰) for a weekly series, 5.21 ‰ (MBE = -3.72 ‰) for a biweekly series, and 7.83  
338 ‰ (MBE = -6.02 ‰) for a monthly series. The  $\delta^{18}\text{O}$   $\hat{\sigma}_1^*$  had RMSEs of 0.35 ‰ (MBE = -0.77 ‰)  
339 for a weekly series, 0.64 ‰ (MBE = -0.48 ‰) for a biweekly series, and 0.98 ‰ (MBE = -0.24  
340 ‰) for a monthly series. For weekly, biweekly and monthly series,  $\hat{\rho}_1^*(\text{P}, \delta^2\text{H})$ ,  $\hat{\rho}_1^*(\text{P}, \delta^{18}\text{O})$ , and  
341  $\hat{\rho}_1^*(\delta^2\text{H}, \delta^{18}\text{O})$  had low RMSEs ranging from 0.01 to 0.18 ‰ and MBEs ranging from -0.01 to  
342 0.03 ‰ across all sites.  $\hat{\rho}_1^*(\text{P}, \delta^2\text{H})$  and  $\hat{\rho}_1^*(\text{P}, \delta^{18}\text{O})$  were more likely to be overestimated for sites  
343 with  $\rho_1^*(\text{P}, \delta^2\text{H})$  and  $\rho_1^*(\text{P}, \delta^{18}\text{O})$  near zero, most likely a result of a site's weak amount effect that  
344 can become less significant and sometimes positive as a time series is aggregated. More data could  
345 improve estimates of  $\hat{\rho}_1^*$ . The *Discussion* provides further detail on methods for potentially  
346 improving statistical estimates at sites where errors were more apparent.

347

#### 348 b. Evaluation of the Downscaled Tracer Realizations

349 The average of each ensemble's means ( $\overline{\hat{\mu}_1}$ ) and standard deviations ( $\overline{\hat{\sigma}_1}$ ) for each isotope  
350 ratio and the Pearson correlation coefficients ( $\overline{\hat{\rho}_1}$ ) between precipitation amount and its  
351 corresponding isotope ratios were compared to the observed daily statistics at each site before



352 applying the residual correction (Figure 4). The downscaled time series with the most accurate  $\widehat{\rho}_1$   
353 were calculated when the method was applied to a weekly time series. After applying a residual  
354 correction on each realization in an ensemble, the residual corrected downscaled series accurately  
355 captured the  $\mu_1$ ,  $\sigma_1$ , and  $\rho_1$  (Figure 5), though slightly altered  $R^2$  values. The  $R^2$  between  $\mu_1$  and  $\widehat{\mu}_1$   
356 and  $\sigma_1$  and  $\widehat{\sigma}_1$  were similar for the original downscaled (Figure 4.a-d) and residual corrected  
357 ensembles (Figure 5.a-d). The residual correction increases the  $R^2$  between  $\rho_1$  and  $\widehat{\rho}_1$  (Figure 4.e-  
358 g, Figure 5.e-g), especially when it is applied on a downscaled weekly series. For a downscaled  
359 weekly series, the  $R^2$  of  $\rho_1(P, \delta^2H)$  and  $\widehat{\rho}_1(P, \delta^2H)$  and  $\rho_1(P, \delta^{18}O)$  and  $\widehat{\rho}_1(P, \delta^{18}O)$  increased  
360 from 0.88 to 0.93 with a residual correction. For applications where model outputs are directly  
361 compared to observation datasets, a residual correction should be applied to generate tracer  
362 ensembles which are comparable to the coarser resolution observed values. The average bias  
363 between the downscaled and observed time series means and standard deviations were summarized  
364 in Table 1. The residual correction on the downscaled ensembles reduced bias in the standard  
365 deviations, but had little effect on the means. The *Discussion* provides further detail on potential  
366 methods for adding informative covariates (e.g. air temperature) to the downscaled time series  
367 estimates at sites where errors were more apparent.

368

### 369 *c. Conserved Processes with the Method*

370 An analysis of the observed time series demonstrates strong autocorrelation; when the  
371 seasonal signal is removed, the observed autocorrelation is nearly all removed (Figure 6). In fact,  
372 the median autocorrelation of the observed time series stochastic signals falls below 5 % after 3-  
373 day lags and are approximately zero at 4-day lags, supporting the assumption that the sinusoidal  
374 function adequately described the deterministic component and the residual was stationary (i.e.

375 white noise). The Shapiro-Wilk and the D'Agostino's  $K^2$  normality tests suggest that we could not  
376 reject the assumption of normality in the weekly, biweekly and monthly time series (p-value >  
377 0.05). Histograms of the stochastic signals for both isotope ratios across all 27 sites are provided  
378 in the *Supplemental Materials* (Figure S3). Next, we calculated autocorrelations from 1- to 20-day  
379 lags of the residual corrected downscaled ensembles. The autocorrelations mimicked the observed  
380 temporal trends and memory of the daily time series. Autocorrelations for  $\delta^2\text{H}$  and  $\delta^2\text{H}^*$  (Figure  
381 6) and are highly correlated with trends observed in the autocorrelations for  $\delta^{18}\text{O}$  and  $\delta^{18}\text{O}^*$  (refer  
382 to *Supplemental Materials*, Figure S4). Based on the results from the autocorrelation analysis and  
383 normality tests, we concluded the addition of the seasonal signal to the generated stochastic time  
384 series captured the large majority of the observed tracer memory in the system.

385         The means and standard deviations in *d*-excess were accurately captured in the resulting  
386 downscaled time series (Figure 7). At each site, *d*-excess was calculated for the observed daily  
387 series and each ensemble from the downscaled weekly, biweekly and monthly time scales. The  
388 downscaled *d*-excess was over-estimated for the three sites with lowest observed *d*-excess,  
389 indicating potential effects to the downscaling method's performance when precipitation is  
390 predominantly composed of evaporated waters. These *d*-excess estimates provide a metric for  
391 evaluating the downscaled series relative to the GMWL and increases the applicability of this  
392 method for tracing meteorological forcing variables and their constituents through modeling  
393 environments. Alternative downscaling approaches that independently model  $\delta^2\text{H}$  and  $\delta^{18}\text{O}$  may  
394 not preserve *d*-excess signals and thus would provide precipitation predictions that should not be  
395 used in simulations that leverage the information provided by dual-isotope analyses.

396

#### 397 **4. Discussion**

398 *a. Method Evaluation for Select Site Characteristics*

399 We compared the absolute error, calculated by taking the absolute value of the mean of the  
400 downscaled ensembles minus the observed mean, to the site's latitude, calculated rainfall  
401 frequency ( $\lambda$ ), and total length of the time series in years (Figure 8). The largest absolute errors of  
402 the mean resulted from downscaling calculations that used monthly aggregated data, yielding  
403 average (+/- standard deviation) absolute errors of 2.26 ‰ (2.54 ‰) for  $\delta^2\text{H}$  and 0.33 ‰ (0.35 ‰)  
404 for  $\delta^{18}\text{O}$ . Linear regressions between site latitude and absolute errors in the means (derived from  
405 monthly, biweekly, and weekly ensembles) showed no strong correlations, suggesting that  
406 performance may be partially climate independent (Figure 8). Absolute errors were also not related  
407 to the strength of the seasonal isotopic variation, nor were they related to the overall variability in  
408 isotopic composition (as quantified by the standard deviation; Figure 9). Alternatively, a weak, but  
409 significant relationship was observed between absolute error and  $\lambda$  ( $R^2 = 0.25$  and p-value = 0.0001  
410 for  $\delta^2\text{H}$ ,  $R^2 = 0.23$  and p-value = 0.0002 for  $\delta^{18}\text{O}$ ) and average recorded precipitation amount ( $R^2$   
411 = 0.12 and p-value = 0.009 for  $\delta^2\text{H}$ ,  $R^2 = 0.13$  and p-value = 0.0003 for  $\delta^{18}\text{O}$ ) for downscaled  
412 weekly ensembles, but not for downscaled biweekly or monthly ensembles (Figures 8 and 9).  
413 Although not a site characteristic, time-series length significantly influenced absolute errors of  
414 downscaled biweekly and monthly ensembles. Longer time series spanning many years support  
415 better accounting for interannual variability and removing potential biases towards certain seasons.  
416 Nonlinear effects (e.g., continentality (Dansgaard 1964, Rozanski et al., 1993)) may be  
417 contributing to relatively high absolute errors, especially at the subtropics and mid-latitudes  
418 (Figure 8.a-b). When applying the downscaling method to datasets from these regions, one can  
419 adapt the copula framework to account for other influential site-specific characteristics (refer to  
420 *Section 2.b*).

421

422 *b. Method Adaptation for Broader Applications*

423         In this study, weekly, biweekly, and monthly data were used to generate daily observations,  
424 but more sophisticated applications could potentially be supported by different datasets. As a  
425 general rule, the deterministic time series component can be more accurately estimated with  
426 increased tracer sampling frequencies (Figure 8.c-d) and samples collected over longer time frames  
427 (Figure 8.e-f). Accurately representing the deterministic component increases the likelihood of a  
428 downscaled synthetic time series effectively representing the underlying seasonal patterns and  
429 interannual variability at a site. Depending on the application, one may increase or decrease the  
430 temporal downscaling intervals beyond daily or 12-week timescales. While not evaluated in this  
431 study, one could predict sub-daily datasets with appropriate observation datasets or known  
432 statistical properties (i.e., mean, standard deviation, covariance structure of precipitation and its  
433 tracer composition) of a site at sub-daily scales (e.g., diurnal cycle).

434         Theoretically, the downscaling methods used in this study can be expanded to higher  
435 dimensions and account for other tracer covariates including site conditions such as air temperature  
436 and relative humidity. At sites where the method under or overestimates the site statistics, other  
437 meteorological variables, such as air temperature, may correlate more strongly with isotope signals  
438 than precipitation amount. To do this, one needs to increase the number of covariates accounted  
439 for and the matrix dimensions within the copula framework (refer to *Supplemental Materials (i)*  
440 *Definition of a Gaussian Copula*). In these instances, adding more known dimensions to Equations  
441 6 and 7 will incorporate additive information into the generated downscaled time series. Including  
442 additional known covariates within the copula framework may improve the representation of  
443 nonlinear effects at sites in the subtropics and mid-latitudes if meteorological variables (e.g.,

444 relative humidity, air temperature) are highly correlated with changes in tracer concentrations  
445 (Figures 8.a-b).

446 Not only would a downscaled time series facilitate running more detailed models that  
447 improve process understanding, but they also allow for better tracking of uncertainties associated  
448 with inferences drawn from those models. We compared the mean of the observed biweekly series  
449 and the mean of the downscaled biweekly ensemble aggregated to biweekly time scales using Eq.  
450 2. The absolute error of the mean across all sites was 0.90 ‰ for  $\delta^2\text{H}$  and 0.14 ‰ for  $\delta^{18}\text{O}$ . This  
451 suggests models using downscaled tracers would mimic temporal trends observed at biweekly time  
452 scales, while also tracking processes and uncertainties only discernible at finer time scales. As  
453 expected, when the residual corrected downscaled biweekly ensemble was aggregated to biweekly  
454 time scales, the absolute error of the mean was approximately zero. To evaluate how the  
455 downscaling method compared to a naive downscale with no high-frequency statistical  
456 information, we created a daily time series where all precipitation events that occurred within each  
457 14-day interval had the same isotopic composition equal to the observed biweekly values. The  
458 absolute error of the mean across all sites (+/- standard deviation) was 2.74 ‰ (2.24 ‰) for  $\delta^2\text{H}$   
459 and 0.39 ‰ (0.31 ‰) for  $\delta^{18}\text{O}$ , which was higher than the absolute error of the mean calculated  
460 for all the downscaled biweekly ensembles (1.69 ‰ (1.61 ‰) for  $\delta^2\text{H}$  and 0.23 ‰ (0.24 ‰) for  
461  $\delta^{18}\text{O}$ ).

462 Due to limited data, all of the above analyses used the entire dataset to calculate the  
463 statistics, fit the models and apply the downscaling method. At sites with more than 5 years of  
464 data, we used the first 4 years to build a downscaling model to apply on the 5<sup>th</sup> year's precipitation  
465 time series. We generated an ensemble of 100 downscaled  $\delta^2\text{H}$  and  $\delta^{18}\text{O}$  time series at each site  
466 and compared it to the observed  $\delta^2\text{H}$  and  $\delta^{18}\text{O}$  from the 5<sup>th</sup> year of the time series. Based on

467 training and testing sizes, eight sites were used in this analysis and the absolute error of the mean  
468 (+/- standard deviation) for  $\delta^2\text{H}$  was 4.80 ‰ (3.17 ‰), 4.89 ‰ (3.26 ‰) and 5.52 ‰ (3.50 ‰)  
469 downscaled from weekly, biweekly, and monthly series, respectively. The absolute error of the  
470 mean (+/- standard deviation) for  $\delta^{18}\text{O}$  was 0.79 ‰ (0.59 ‰), 0.78 ‰ (0.63 ‰) and 0.85 ‰ (0.67  
471 ‰) downscaled from weekly, biweekly, and monthly series, respectively. Based on these  
472 promising results, our downscaling method could be built using several years of precipitation data  
473 with a known concentration and then applied to years where only precipitation amount is available.

474 This method can be broadly applied to produce ensembles of downscaled datasets for  
475 various geochemical modeling applications. Ensembles decrease the risk of tying conclusions to  
476 one specific time series. The downscaled ensembles can be generated using the same statistics  
477 (like shown here) or multiple ensembles can be generated with varying statistical properties.  
478 Examples of different ensembles include time series generated from downscaled statistics  
479 estimated from different aggregation intervals (e.g. weekly and biweekly), employing a non-  
480 Gaussian copula framework (e.g. Gumbel copula, Extreme-value copula) to populate a conditioned  
481 stochastic signal's time series, and increasing dimensions of the copula framework by including  
482 additive meteorological variables (e.g. air temperature). Correspondingly, the geochemical tracer  
483 ensembles could be used for model selection and with numerous model and parameter sensitivity  
484 and uncertainty analyses. Ensembles could be useful in developing frameworks for model-data  
485 fusion by merging observational data with model outputs to improve model quality and  
486 characterize its uncertainty.

487 This downscaling approach could be extended across large spatial extents for use in global  
488 isotopic models or empirically based geographic simulations to represent sites with limited or no  
489 high-frequency observations available. To do this, one could generate downscaled geochemical

490 tracers correlating with precipitation inputs at the grid-scale. Lastly, the methodology can be  
491 applied to other geochemical tracers for understanding site-specific dynamics (e.g. chemical  
492 leaching, sediment transport and loading) or climatological applications (e.g. nitrogen deposition,  
493 carbon sequestration).

494

## 495 **5. Conclusions**

496 This statistical downscaling method generates datasets that maintain informative site-  
497 specific correlation structures between covariates and the geochemical tracer and retains the  
498 statistical properties of underlying processes (e.g., *d*-excess, amount effects). By modeling  
499 hydrologic dynamics using downscaled tracers, researchers can enhance understanding of physical  
500 processes without collecting fine temporal in-situ data. While an individual realization of this  
501 downscaling approach may generate reasonable estimates of true high-frequency values, iterating  
502 analyses using an ensemble of realizations allows for uncertainties in generated time series to be  
503 propagated through subsequent modeling and tracer-based analyses. The method is sufficiently  
504 general and can be applied for a variety of applications to generate downscaled ensembles for use  
505 in meteorological and hydrometeorological models to evaluate model performance, investigate  
506 system processes across spatial scales and is additive to model-data fusion frameworks.

507

## 508 *Acknowledgements*

509 The authors acknowledge the support of the United States National Science Foundation  
510 (DEB-1802885, DEB-1802880 and AGS-1954660) and thank the anonymous reviewers for their  
511 time and effort spent reviewing this manuscript. The authors state no conflict of interest.

512

513 *Data Availability Statement*

514 Python code is provided in the *Supplemental Material* to generate geochemical synthetic  
515 time series based on the user's site-specific time series statistics. The code is intended to be easily  
516 adaptable to higher dimensions or other user specific applications. Additional materials can be  
517 made available upon request.

518

519

#### REFERENCES

520 Abbott, B. W., V. Baranov, C. Mendoza-Lera, M. Nikolakopoulou, A. Harjung, T. Kolbe, M. N.  
521 Balasubramanian, T. N. Vaessen, F. Ciocca, A. Campeau, M. B. Wallin, P. Romeijn, M. Antonelli,  
522 J. Gonçalves, T. Datry, A. M. Laverman, J. de Dreuzy, D. M. Hannah, S. Krause, C. Oldham, and  
523 G. Pinay, 2016: Using multi-tracer inference to move beyond single catchment ecohydrology.  
524 *Earth-Sci. Rev.*, **160**, 19-42, <https://doi.org/10.1016/j.earscirev.2016.06.014>.

525

526 Aggarwal, P. K., O. A. Alduchov, K. O. Froehlich, L. J. Araguas-Araguas, N. C. Sturchio, and N.  
527 Kurita, 2012: Stable isotopes in global precipitation: a unified interpretation based on atmospheric  
528 moisture residence time. *Geophys. Res. Lett.*, **39**, 1-6, <https://doi.org/10.1029/2012GL051937>.

529

530 Aggarwal, P. K., U. Romatschke, L. Araguas-Araguas, D. Belachew, F. J. Longstaffe, P. Berg, C.  
531 Schumacher, and A. Funk, 2016: Proportions of convective and stratiform precipitation revealed  
532 in water isotope ratios. *Nat. Geosci.*, **9**, 624-629, <https://doi.org/10.1038/ngeo2739>.

533



534 Allen, S. T., Jasechko, S., Berghuijs, W. R., Welker, J. M., Goldsmith, G. R., and Kirchner, J. W.,  
535 2019: Global sinusoidal seasonality in precipitation isotopes, *Hydrol. Earth Syst. Sci.*, **23**, 3423–  
536 3436, <https://doi.org/10.5194/hess-23-3423-2019>.  
537  
538 Allen, S. T., Kirchner, J. W., & Goldsmith, G. R., 2018. Predicting spatial patterns in precipitation  
539 isotope ( $\delta^2\text{H}$  and  $\delta^{18}\text{O}$ ) seasonality using sinusoidal isoscapes. *Geophys. Res.*, **45**, 4859–4868,  
540 <https://doi.org/10.1029/2018GL077458>.  
541  
542 Bailey, A., E. Posmentier, and X. Feng, 2018: Patterns of Evaporation and Precipitation Drive  
543 Global Isotopic Changes in Atmospheric Moisture. *Geophys. Res. Lett.*, **45**, 7093-7101,  
544 <https://doi.org/10.1029/2018GL078254>.  
545  
546 Bárdossy, A. and G. G. S. Pegram, 2009: Copula based multisite model for daily precipitation  
547 simulation. *Hydrol. Earth Syst. Sci.*, **13**, 2299-2314.  
548  
549 Benetti, M., G. Reverdin, C. Pierre, L. Merlivat, C. Risi, H. C. Steen-Larsen, and F. Vimeux, 2014:  
550 Deuterium excess in marine water vapor: Dependency on relative humidity and surface wind speed  
551 during evaporation. *J. Geophys. Res-Atmos.*, **119**, 583-593,  
552 <https://doi.org/10.1002/2013JD020535>.  
553  
554 Brady, E., Stevenson, S., Bailey, D., Liu, Z., Noone, D., Nusbaumer, J., Otto-Bliesner, B.  
555 L., Tabor, C., Tomas, R., Wong, T., et al., 2019: The Connected Isotopic Water Cycle in the

556 Community Earth System Model Version 1. *J. Adv. Model. Earth Syst.*, **11**, 2547–2566,  
557 <https://doi.org/10.1029/2019MS001663>.  
558  
559  
560 Brooks, J. R., J. J. Gibson, S. J. Birks, M. H. Weber, K. D. Rodecap, and J. L. Stoddard, 2014:  
561 Stable isotope estimates of evaporation: inflow and water residence time for lakes across the  
562 United States as a tool for national lake water quality assessments. *Limnol. Oceanogr.*, **59**, 2150-  
563 2165, <https://doi.org/10.4319/lo.2014.59.6.2150>.  
564  
565 Bordoy, R. and P. Burlando, 2013: Stochastic downscaling of climate model precipitation outputs  
566 in orographically complex regions: 2. Downscaling methodology. *Water Resour. Res.*, **50**, 562-  
567 579, <https://doi.org/10.1002/wrcr.20443>.  
568  
569 Bowen, G. J., Z. Cai, R. P. Fiorella, and A. L. Putman, 2019: Isotopes in the water cycle: Regional-  
570 to global-scale patterns and applications. *Annu. Rev. Earth Planet Sci.*, **47**, 453-479,  
571 <https://doi.org/10.1146/annurev-earth-053018-060220>.  
572  
573 Bowen, G. J. and S. P. Good, 2015: Incorporating water isotopes in hydrological and water  
574 resource investigations. *WIREs. Water*, **2**, 2, 107-119. <https://doi.org/10.1002/wat2.1069>.  
575  
576 Celle-Jeanton, H. Y. Travi, and B. Blavoux, 2001: Isotopic typology of the precipitation in the  
577 Western Mediterranean region at three different time scales. *Geophys. Res. Lett.*, **28**, 7, 1215-1218,  
578 <https://doi.org/10.1029/2000GL012407>.

579

580 Clow, D. W., M. A. Mast, and J. O. Sickman, 2018: Linking transit times to catchment sensitivity  
581 to atmospheric deposition of acidity and nitrogen in mountains of the western United States,  
582 *Hydrol. Process*, **32**, 16, 2456–2470, <https://doi.org/10.1002/hyp.13183>.

583

584 Cong, R. and M. Brady, 2012: The interdependence between rainfall and temperature: copula  
585 analysis. *The Scientific World Journal*, **2012**, 1-11, <https://doi.org/10.1100/2012/405675>.

586

587 Conroy, J. L., Noone, D., Cobb, K. M., Moerman, J. W., and Konecky, B. L. (2016), Paired stable  
588 isotopologues in precipitation and vapor: A case study of the amount effect within western tropical  
589 Pacific storms, *J. Geophys. Res. Atmos.*, **121**, 3290– 3303,  
590 <https://doi.org/10.1002/2015JD023844>.

591

592 Coulibaly, P., Y. B. Dibike, and F. Anctil, 2005: Downscaling precipitation and temperature with  
593 temporal neural networks. *J. Hydrometeor.*, **6**, 483-496, <https://doi.org/10.1175/JHM409.1>.

594

595 Craig, H., 1961: Isotopic variations in meteoric waters. *Science*, **133**, 1702-1703.

596

597 Craig, H. and L. I. Gordon, 1965: Deuterium and oxygen-18 variations in the ocean and the marine  
598 atmosphere. In *E. Tongiorgi, ed*, Proceedings of a Conference on Stable Isotopes in Oceanographic  
599 Studies and Paleotemperatures, Spoleto, Italy, pp 9-130.

600

601 Dansgaard, W., 1964: Stable isotopes in precipitation. *Tellus*, **16**, 436–468,  
602 <https://doi.org/10.1111/j.2153-3490.1964.tb00181.x>.

603

604 D’Onofrio, D. 2014: Stochastic rainfall downscaling of climate models. *J. Hydrometeor.*, **15**, 830-  
605 843, <https://doi.org/10.1175/JHM-D-13-096.1>.

606

607 Dutton, A., B. H. Wilkinson, J. M. Welker, G. J. Bowen, and K. C. Lohmann, 2005: Spatial  
608 distribution and seasonal variation in  $^{18}\text{O}/^{16}\text{O}$  of modern precipitation and river water across the  
609 conterminous USA, *Hydrol. Process.*, **19**, 20, 4121–4146, <https://doi.org/10.1002/hyp.5876>.

610

611 Ebtehaj, A. M., and E. Foufoula-Georgiou, 2013: On variational downscaling, fusion, and  
612 assimilation of hydrometeorological states: A unified framework via regularization. *Water Resour.*  
613 *Res.*, **49**, 5944– 5963, <https://doi.org/10.1002/wrcr.20424>.

614

615 Fekete, B. M., J. J. Gibson, P. Aggarwal, C. J. Vörösmarty, 2006: Application of isotopic tracers  
616 in continental scale hydrological modeling. *J. Hydrol.*, **330**, 3-4, 444-456,  
617 <https://doi.org/10.1016/j.jhydrol.2006.04.029>.

618

619 Feng, X., A. M. Faiia, and E. S. Posmentier, 2009: Seasonality of isotopes in precipitation: A  
620 global perspective. *J. Geophys. Res-Atmos*, **114**, D8, <https://doi.org/10.1029/2008JD011279>.

621

622 v. Freyberg, J., S. T. Allen, S. Seeger, M. Weiler, and J. W. Kirchner, 2018: Sensitivity of young  
623 water fractions to hydroclimatic forcing and landscape properties across 22 Swiss catchments,  
624 *Hydrol. Earth Syst. Sci.*, **22**, 7, 3841–3861, <https://doi.org/10.5194/hess-22-3841-2018>.  
625

626 Fröhlich K., J. J. Gibson, and P. K. Aggarwal, 2002: Deuterium excess in precipitation and its  
627 climatological significance. Study of environmental change using isotope techniques. *C&S Papers*  
628 *Series*, **13**, 54-65. International Atomic Energy Agency: Vienna, Austria.  
629

630 Gallart, F., M. Valiente, P. Llorens, C. Cayuela, M. Sprenger, and J. Latron, 2020: Investigating  
631 young water fractions in a small Mediterranean mountain catchment: both precipitation forcing  
632 and sampling frequency matter. *Hydrol. Processes*, <https://doi.org/10.1002/hyp.13806>.  
633

634 Gao, C., Y. Xu, Q. Zhu, Z. Bai, and L. Liu, 2018: Stochastic generation of daily rainfall events: a  
635 single-site rainfall model with copula-based joint simulation of rainfall characteristics and  
636 classification and simulation of rainfall patterns. *J. Hydrol.*, **564**, 41-58,  
637 <https://doi.org/10.1016/j.jhydrol.2018.06.073>.  
638

639 Gat, J. R., 1996: Oxygen and hydrogen isotopes in the hydrologic cycle. *Annu. Rev. Earth Planet*  
640 *Sci.*, **24**, 225-262, <https://doi.org/10.1146/annurev.earth.24.1.225>.  
641

642 Gibson, J. J., T. W. D. Edwards, S. J. Birks, N. A. St Amour, W. M. Buhay, P. McEachern, B. B.  
643 Wolfe, and D. L. Peters, 2005: Progress in isotope tracer hydrology in Canada. *Hydrol. Process.*,  
644 **19**, 1, 303-327, <https://doi.org/10.1002/hyp.5766>.

645

646 Goncu, S., and E. Albek, 2016: Statistical downscaling of meteorological time series and climatic  
647 projections in a watershed in Turkey. *Theoretical and Applied Climatology*, **126**, 1-2,  
648 <https://link.gale.com/apps/doc/A470736525/AONE?u=s8405248&sid=AONE&xid=e894de9e>.

649

650 Good S. P., D. V. Mallia, J. C. Lin, and G. J. Bowen, 2014: Stable isotope analysis of precipitation  
651 samples obtained via crowdsourcing reveals the spatiotemporal evolution of superstorm sandy.  
652 *PLOS ONE* **9**, 3, e91117, <https://doi.org/10.1371/journal.pone.0091117>.

653

654 Good, S. P., D. Noone, and G. Bowen, 2015: Hydrologic connectivity constrains partitioning of  
655 global terrestrial water fluxes. *Science*, **349**, 175-177, <https://doi.org/10.1126/science.aaa5931>.

656

657 Gupta, A., E. P. Gerber, and P. H. Lauritzen, 2020: Numerical impacts on tracer transport: A  
658 proposed intercomparison test of Atmospheric General Circulation Models. *Q. J. R. Meteorol.*  
659 *Soc.*, **146**, 3937– 3964, <https://doi.org/10.1002/qj.3881>.

660

661 Gyasi-Agyei, Y., 2011: Copula-based daily rainfall disaggregation model. *Water Resour. Res.*, **47**,  
662 W07535, <https://doi.org/10.1029/2011WR010519>.

663

664 Halder, J., S. Terzer, L. I. Wassenaar, L. J. Araguás-Araguás, and P. K. Aggarwal, 2015: The  
665 Global Network of Isotopes in Rivers (GNIR): integration of water isotopes in watershed  
666 observation and riverine research. *Hydrol. Earth Syst. Sci.*, **19**, 8, 3419–3431,  
667 <https://doi.org/10.5194/hess-19-3419-2015>.

668

669 Haslauer, C. P., P. Guthke, A. Bádosy, and E. A. Sudicky, 2012: Effects of non-gaussian copula-  
670 based hydraulic conductivity fields on macrodispersion. *Water Resour. Res.*, **48**, 1-18,  
671 <https://doi.org/10.1029/2011WR011425>.

672

673 Hoffmann, G., J. Jouzel and V. Masson, 2000: Stable water isotopes in atmospheric general  
674 circulation models. *Hydrol. Processes*, **14**, 1385-1406, [https://doi.org/10.1002/1099-1085\(20000615\)14:8<1385::AID-HYP989>3.0.CO2-1](https://doi.org/10.1002/1099-1085(20000615)14:8<1385::AID-HYP989>3.0.CO2-1).

675

676

677 Huang, J., J. Zhang, Z. Zhang, S. Sun and J. Yao, 2012: Simulation of extreme precipitation indices  
678 in the Yangtze River basin by using statistical downscaling method (SDSM). *Theor. Appl. Climatol.* **108**, 325–343, <https://doi.org/10.1007/s00704-011-0536-3>.

679

680

681 IAEA/WMO (2020). Global Network of Isotopes in Precipitation. The GNIP Database. Accessible  
682 at: <http://www.iaea.org/water>.

683

684 Ingraham, N. L., 1998: Isotopic variations in precipitation. In C. Kendall & J. J. McDonnell (Eds.),  
685 *Isotope Tracers in Catchment Hydrology* (pp. 87–118). Amsterdam: Elsevier Science,  
686 <https://doi.org/10.1016/B978-0-444-81546-0.50010-0>.

687

688 Jacobs, S. R., E. Timbe, B. Weeser, M. C. Rufino, K. Butterbach-Bahl, and L. Breuer, 2018:  
689 Assessment of hydrological pathways in East African montane catchments under different land  
690 use. *Hydrol. Earth Syst. Sci.*, **22**, 4981-5000, <https://doi.org/10.5194/hess-22-4981-2018>.

691  
692 Jasechko, S. and R. Taylor, 2015: Intensive rainfall recharges tropical groundwaters. *Environ. Res.*  
693 *Lett.*, **10**, <https://doi.org/10.1088/1748-9326/10/12/124015>.  
694  
695 Jasechko, S., J. W. Kirchner, J. M. Welker, and J. J. McDonnell, 2016: Substantial proportion of  
696 global streamflow less than three months old. *Nat. Geosci.*, **9**, 2, 126–129,  
697 <https://doi.org/10.1038/ngeo2636>.  
698  
699 Kanner, L. C., N. H. Buenning, L. D. Stott, A. Timmermann, and D. Noone, 2014: The role of soil  
700 processes in  $\delta^{18}O$  terrestrial climate proxies. *Global Biogeochem. Cycles*, **28**, 239-252,  
701 <https://doi.org/10.1002/2013GB004742>.  
702  
703 Kendall, C. and J. J. McDonnell, 2012: *Isotope tracers in catchment hydrology*. Elsevier, 870pp.  
704  
705 Khedun, C. P., A. K. Mishra, V. P. Singh and J. R. Giardino, 2014: A copula-based precipitation  
706 forecasting model: investigating the interdecadal modulation of ENSO's impacts on monthly  
707 precipitation. *Water Resour. Res.*, **50**, 580-600, <https://doi.org/10.1002/2013WR013763>.  
708  
709 Kirchner, J. W., 2016a: Aggregation in environmental systems—Part 1: Seasonal tracer cycles  
710 quantify young water fractions, but not mean transit times, in spatially heterogeneous catchments.  
711 *Hydrol. Earth Syst. Sci.*, **20**, 1, 279–297, <https://doi.org/10.5194/hess-20-279-2016>.  
712



713 Kirchner, J. W., 2016b: Aggregation in environmental systems—Part 2: Catchment mean transit  
714 times and young water fractions under hydrologic nonstationarity. *Hydrol. Earth Syst. Sci.*, **20**, 1,  
715 299–328, <https://doi.org/10.5194/hess-20-299-2016>.

716

717 Konecky, B. L., D. C. Noone, and K. M. Cobb, 2019: The influence of competing hydroclimate  
718 processes on stable isotope ratios in tropical rainfall. *Geophys. Res. Lett.*, **46**, 1622-1633,  
719 <https://doi.org/10.1029/2018GL080188>.

720

721 Krause, P., D. P. Boyle, and F. Bäse, 2005: Comparison of different efficiency criteria for  
722 hydrological model assessment. *Adv. in Geosci.*, **5**, 89-97, [https://doi.org/1680-7359/adgeo/2005-](https://doi.org/1680-7359/adgeo/2005-5-89)  
723 5-89.

724

725 Kuhn, G., S. Khan, A. R. Ganguly, and M. L. Branstetter, 2007: Geospatial-temporal dependence  
726 among weekly precipitation extremes with applications to observations and climate model  
727 simulations in South America. *Adv. Water Resour.*, **30**, 2401-2423,  
728 <https://doi.org/10.1016/j.advwatres.2007.05.006>.

729

730 Laux, P., S. Vogl, W. Qiu, H. R. Knoche, and H. Kunstmann, 2011: Copula-based statistical  
731 refinement of precipitation in RCM simulations over complex terrain. *Hydrol. Earth Syst. Sci.*, **15**,  
732 2401-2419, <https://doi.org/10.5194/hess-15-2401-2011>.

733

734 Laux, P., S. Wagner, A. Wagner, J. Jacobeit, A. Bárdossy, and H. Kunstmann, 2009: Modelling  
735 daily precipitation features in the Volta Basin of West Africa. *International Journal of*  
736 *Climatology*, **29**, 937-954, <https://doi.org/10.1002/joc.1852>.  
737  
738 Lee, J. E. and I. Fung, 2008: “Amount effect” of water isotopes and quantitative analysis of post-  
739 condensation processes. *Hydrol. Process.*, **22**, 1-8, <https://doi.org/10.1002/hyp.6637>.  
740  
741 Lutz, S. R., R. Krieg, C. Müller, M. Zink, K. Knöller, L. Samaniego, and R. Merz, 2018: Spatial  
742 patterns of water age: Using young water fractions to improve the characterization of transit times  
743 in contrasting catchments. *Water Resour. Res.*, **54**, 7, 4767–4784,  
744 <https://doi.org/10.1029/2017WR022216>.  
745  
746 McGuire, K. J. and J. J. McDonnell, 2006: A review and evaluation of catchment transit time  
747 modeling. *J. Hydrol.*, **330**, 543-563, <https://doi.org/10.1016/j.jhydrol.2006.04.020>.  
748  
749 Moerman, J. W., K. M. Cobb, J. F., Adkins, H. Sodemann, B. Clark, and A. A. Tuen, 2013: Diurnal  
750 to interannual rainfall  $\delta^{18}O$  variations in northern Borneo driven by regional hydrology. *Earth*  
751 *Planet. Sci. Lett.*, **369-370**, 108-109, <https://doi.org/10.1016/j.epsl.2013.03.014>.  
752  
753 Moore, M., Kuang, Z., and Blossey, P. N., 2014: A moisture budget perspective of the amount  
754 effect, *Geophys. Res. Lett.*, **41**, 1329– 1335, <https://doi.org/10.1002/2013GL058302>.  
755

756 Moore, M., P. N. Blossey, A. Muhlbauer, and Z. Kuang, 2016: Microphysical controls on the  
757 isotopic composition of wintertime orographic precipitation. *J. Geophys. Res. Atmos.*, **121**, 7235-  
758 7253, <https://doi.org/10.1002/2015JD023763>.

759  
760 Nusbaumer, J., T. E. Wong, C. Bardeen, and D. Noone, 2017: Evaluating hydrological processes  
761 in the Community Atmosphere Model Version 5 (CAM5) using stable isotope ratios of water. *J.*  
762 *Adv. Model Earth Sy.*, **9**, 2, 949-977, <https://doi.org/10.1002/2016MS000839>.

763  
764 Orbe, C., D. Rind, J. Jonas, L. Nazarenko, G. Faluvegi, L. T. Murray, D. T. Shindell, K. Tsigaridis,  
765 T. Zhou, M. Kelley, and G. A. Schmidt, 2020: GISS Model E2.2: A climate model optimized for  
766 the middle atmosphere—2. Validation of large-scale transport and evaluation of climate response.  
767 *J. Geophys. Res. Atmos.*, **125**, [https://doi-](https://doi-org.ezproxy.proxy.library.oregonstate.edu/10.1029/2020JD033151)  
768 [org.ezproxy.proxy.library.oregonstate.edu/10.1029/2020JD033151](https://doi-org.ezproxy.proxy.library.oregonstate.edu/10.1029/2020JD033151).

769  
770 Pfahl, S. and H. Sodemann, 2014: What controls deuterium excess in global precipitation?. *Clim.*  
771 *Past*, **10**, 771–781, <https://doi.org/10.5194/cp-10-771-2014>.

772  
773 Poduje, A. C. C. and U. Haberlandt, 2017: Short time step continuous rainfall modeling and  
774 simulation of extreme events. *J. Hydrol.*, **552**, 182-197,  
775 <https://doi.org/10.1016/j.jhydrol.2017.06.036>.

776

777 Remondi, F., J. W. Kircher, P. Burlando, and S. Fatichi, 2018: Water flux tracking with a  
778 distributed hydrologic model to quantify controls on the spatio-temporal variability of transit time  
779 distributions. *Water Resour. Res.*, **54**, 4, 3081-3099, <https://doi.org/10.1002/2017WR021689>.

780

781 Risi, C., D. Noone, J. Worden, C. Frankenberg, G. Stiller, M. Kiefer, B. Funke, K. Walker, P.  
782 Bernath, M. Schneider, D. Wunch, V. Sherlock, N. Deutscher, D. Griffith, P. O. Wennberg, K.  
783 Strong, D. Smale, E. Mahieu, S. Barthlott, F. Hase, O. García, J. Notholt, T. Warneke, G. Toon,  
784 D. Sayres, S. Bony, J. Lee, D. Brown, R. Uemura, C. Sturm, 2012: Process-evaluation of  
785 tropospheric humidity simulated by general circulation models using water vapor isotopic  
786 observations: 2. Using isotopic diagnostics to understand the mid and upper tropospheric moist  
787 bias in the tropics and subtropics, *J. Geophys. Res.*, **117**, D05304,  
788 <https://doi.org/10.1029/2011JD016623>.

789

790 Risi, C., S. Bony, S., and F. Vimeux, 2008: Influence of convective processes on the isotopic  
791 composition ( $\delta^{18}\text{O}$  and  $\delta\text{D}$ ) of precipitation and water vapor in the tropics: 2. Physical  
792 interpretation of the amount effect. *J. Geophys. Res.*, **113**, D19306,  
793 <https://doi.org/10.1029/2008JD009943>.

794

795 Rosa, D., Lamarque, J. F., and Collins, W. D. 2012: Global transport of passive tracers in  
796 conventional and superparameterized climate models: Evaluation of multi-scale methods, *J. Adv.*  
797 *Model. Earth Syst.*, **4**, <https://doi.org/10.1029/2012MS000206>.

798

799 Rozanski, K., Araguás- Araguás, L. and Gonfiantini, R. 1993: Isotopic Patterns in Modern Global  
800 Precipitation. *In Climate Change in Continental Isotopic Records* (eds P.K. Swart, K.C. Lohmann,  
801 J. Mckenzie and S. Savin). <https://doi.org/10.1029/GM078p0001>.  
802

803 Schölzel, C. and P. Friederichs, 2008: Multivariate non-normally distributed random variables in  
804 climate research- introduction to the copula approach. *Nonlinear Processes in Geophysics*, **15**,  
805 761-772. <https://doi.org/10.5194/npg-15-761-2008>.  
806

807 Schneider, M. and F. Ramos, 2014: Transductive learning for multi-task copula processes.  
808 *Technical Report*, 1-8, [http://www-](http://www-personal.usyd.edu.au/~framos/Publications_files/TransductiveCopulas.pdf)  
809 [personal.usyd.edu.au/~framos/Publications\\_files/TransductiveCopulas.pdf](http://www-personal.usyd.edu.au/~framos/Publications_files/TransductiveCopulas.pdf).  
810

811 Sklar, A., 1959: Fonctions de répartition à n dimensions et leurs marges. *Publ. Inst. Stat. Univ.*  
812 *Paris*, **8**, 229–231.  
813

814 So, B., J. Kim, H. Kwon, and C. H. R. Lima, 2017: Stochastic extreme downscaling model for an  
815 assessment of changes in rainfall intensity-duration-frequency curves over South Korea using  
816 multiple regional climate models. *J. Hydrol.*, **553**, 321-337,  
817 <https://doi.org/10.1016/j.hydrol.2017.07.061>.  
818

819 Soderberg, K., S. P. Good, L. Wang, and K. Caylor, 2012: Stable isotopes of water vapor in the  
820 vadose zone: a review of measurement and modeling techniques. *Vadose Zone J.*  
821 <https://doi.org/10.2136/vzj2011.0165>.

822

823 Song, C., G. Wang, G. Liu, T. Mao, X. Sun, and X. Chen, 2016: Stable isotope variations of  
824 precipitation and streamflow reveal the young water fraction of a permafrost watershed. *Hydrol.*  
825 *Processes*, **31**, 4, 935–947, doi:10.1002/hyp.11077.

826

827 Sprenger, M., C. Stumpp, M. Weiler, W. Aeschbach, S. T. Allen, P. Benettin, M. Dubbert, A.  
828 Hartmann, M. Hrachowitz, J. W. Kirchner, J. J. McDonnell, N. Orłowski, D. Penna, S. Pfahl, M.  
829 Rinderer, N. Rodriguez, M. Schmidt, and C. Werner, 2019: The demographics of water: A review  
830 of water ages in the critical zone. *Rev. of Geophysics*, **57**, 800-834,  
831 <https://doi.org/10.1029/2018RG000633>.

832

833 Steen-Larsen, H. C., C. Risi, M. Werner, K. Yoshimura, and V. Masson-Delmotte, 2017:  
834 Evaluating the skills of isotope-enabled general circulation models against in situ atmospheric  
835 water vapor isotope observations, *J. Geophys. Res. Atmos.*, **122**, 246–263,  
836 <https://doi.org/10.1002/2016JD025443>.

837

838 Stumpp, C., J. Klaus, and W. Stichler, 2014: Analysis of long-term stable isotopic composition in  
839 German precipitation. *J. Hydrol.*, **517**, 351-361, <https://doi.org/10.1016/j.jhydrol.2014.05.034>.

840

841 Stumpp, C., W. Stichler, M. Kandolf, and J. Šimunek, 2012: Effects of land cover and fertilization  
842 method on water flow and solute transport in five lysimeters: a long-term study using stable water  
843 isotopes. *Vadose Zone J.*, <https://doi.org/10.2136/vzj2011.0075>.

844

845 Tharammal, T., Bala, G., and Noone, D., 2017: Impact of deep convection on the isotopic amount  
846 effect in tropical precipitation, *J. Geophys. Res. Atmos.*, **122**, 1505– 1523,  
847 <http://dx.doi.org/10.1002/2016JD025555>.

848

849 Turnadge, C. and B. D. Smerdon, 2014: A review of methods for modelling environmental tracers  
850 in groundwater: Advantages of tracer concentration simulation. *J. Hydrol.*, **519**,  
851 <http://dx.doi.org/10.1016/j.jhydrol.2014.10.056>.

852

853 Vachon, R. W., J. W. C. White, E. Gutmann, and J. M. Welker, 2007: Amount-weighted annual  
854 isotopic ( $\delta^{18}\text{O}$ ) values are affected by the seasonality of precipitation: A sensitivity study.  
855 *Geophys. Res. Lett.*, **34**, 21, L21707, doi:10.1029/2007GL030547.

856

857 West, J. B., G. J. Bowen, T. E. Dawson, and K. P. Tu, 2010: *Isoscapes: Understanding movement,*  
858 *pattern, and process on Earth through isotope mapping*. Springer, 487pp.

859

860 Wiederhold, J. G., 2015: Metal stable isotope signatures as tracers in environmental geochemistry.  
861 *Environ. Sci. Technol.*, **49**, 2606-2624, <https://doi.org/10.1021/es504683e>.

862

863 Wilkinson, B. H. and L. C. Ivany, 2002: Paleoclimatic inference from stable isotope profiles of  
864 accretionary biogenic hardparts – a quantitative approach to the evaluation of incomplete data,  
865 *Palaeogeogr. Palaeoclimatol. Palaeoecol.*, **185**, 1, 95–114, [https://doi.org/10.1016/S0031-](https://doi.org/10.1016/S0031-0182(02)00279-1)  
866 [0182\(02\)00279-1](https://doi.org/10.1016/S0031-0182(02)00279-1).

867

868 Wong, T. E., J. Nusbaumer, and D. C. Noone, 2017: Evaluation of modeled land-atmosphere  
 869 exchanges with a comprehensive water isotope fractionation scheme in version 4 of the  
 870 Community Land Model. *J. Adv. Model Earth Sy.*, **9**, 2, 978-1001,  
 871 <https://doi.org/10.1002/2016MS000842>.

872

873 Yang, W., A. Bárdossy, and H. J. Caspary, 2010: Downscaling daily precipitation time series  
 874 using a combined circulation- and regression-based approach. *Theor. Appl. Climatol*, **102**, 439-  
 875 454, <https://doi.org/10.1007/s00704-010-0272-0>.

876

877

## TABLES

878 Table 1. Average bias (predicted - observed statistic) (+/- standard deviation) for downscaled and  
 879 *residual corrected downscaled* ensembles

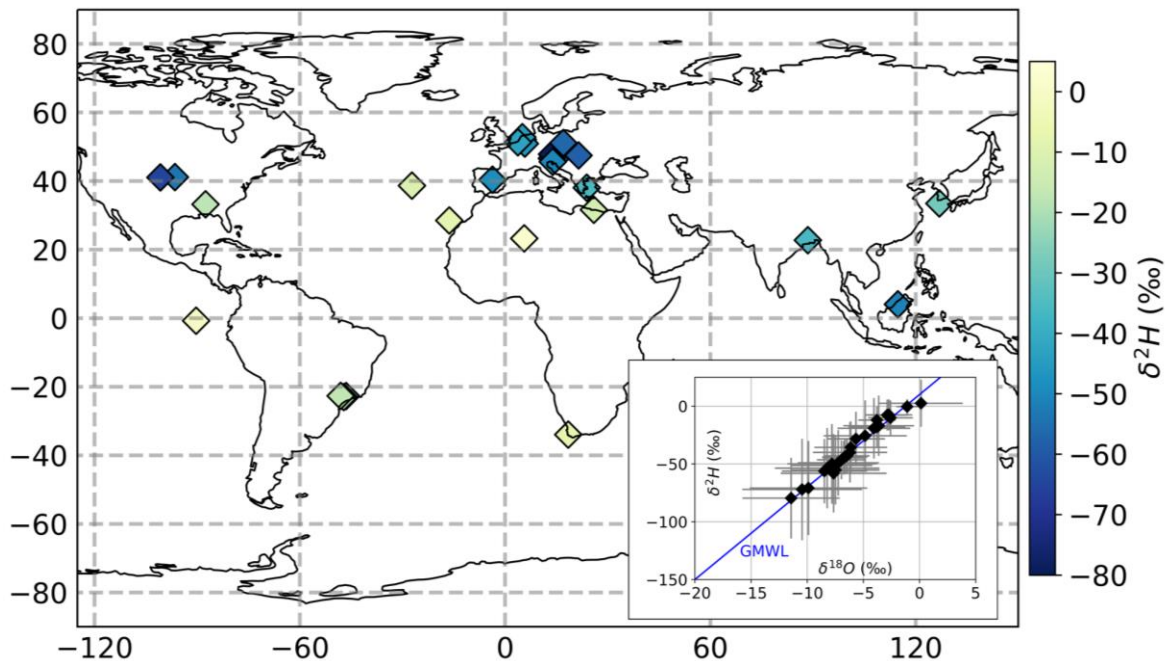
	Bias in the Means (‰)				Bias in the Standard Deviations (‰)			
	$\delta^2\text{H}$	$\delta^2\text{H}$	$\delta^{18}\text{O}$	$\delta^{18}\text{O}$	$\delta^2\text{H}$	$\delta^2\text{H}$	$\delta^{18}\text{O}$	$\delta^{18}\text{O}$
<b>Weekly</b>	-0.10 (1.39)	0.01 (1.79)	-0.02 (0.20)	-0.03 (0.26)	0.02 (2.38)	1.95 (3.30)	0.004 (0.34)	0.25 (0.46)
<b>Biweekly</b>	-1.00 (2.20)	-0.68 (3.50)	-0.16 (0.30)	-0.12 (0.46)	1.04 (3.95)	2.76 (4.14)	0.17 (0.56)	0.39 (0.59)
<b>Monthly</b>	-1.43 (3.08)	-0.13 (5.86)	-0.23 (0.43)	-0.05 (0.74)	2.20 (8.75)	3.28 (8.81)	0.28 (1.12)	0.43 (1.12)

880

881

## FIGURES

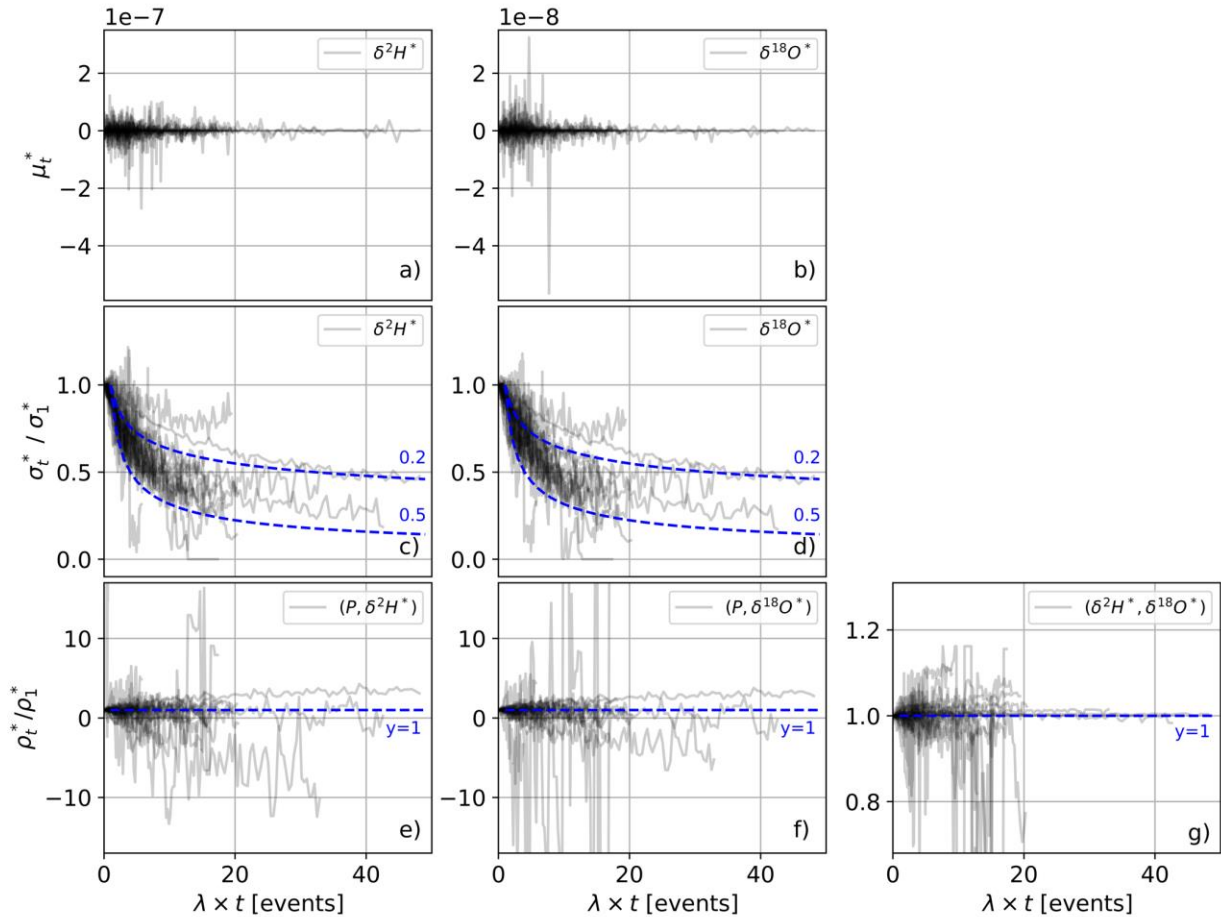




882

883 Figure 1. The large map displays the 27 GNIP site locations and their average  $\delta^2\text{H}$  precipitation  
 884 measurements. The smaller figure is a dual isotope plot with the mean and standard deviations of  
 885 all daily precipitation stable water isotope measurements ( $\delta^2\text{H}$ ,  $\delta^{18}\text{O}$ ) at the 27 GNIP sites. The  
 886 Global Meteoric Water Line (GMWL) is included in the subplot. Refer to Table S1 in the  
 887 *Supplemental Material* for more site-specific characteristics.

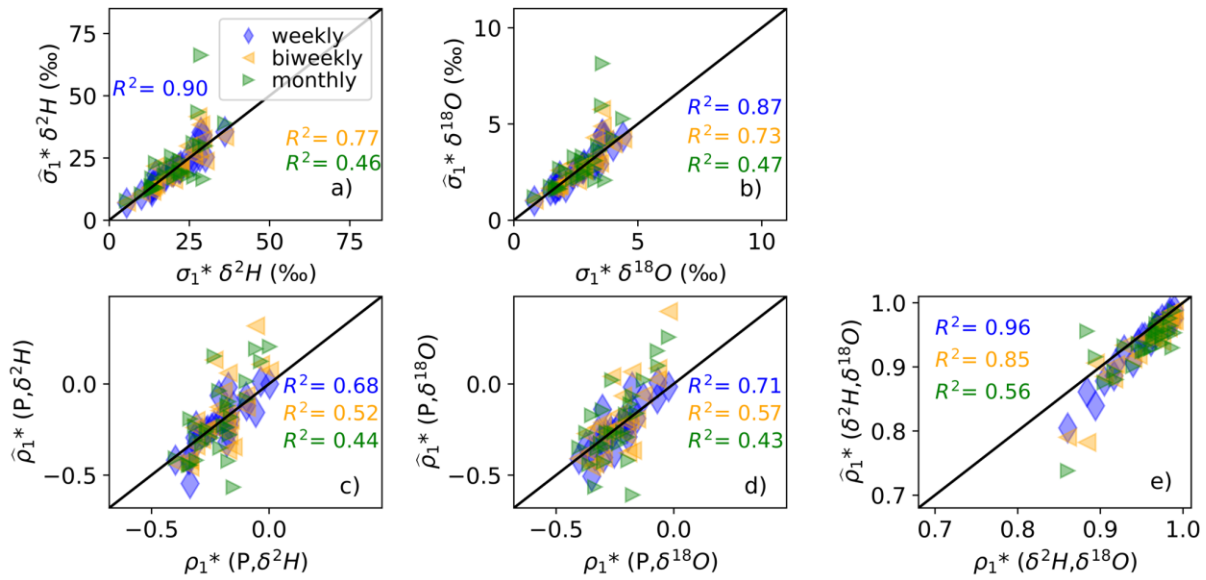
888



889

890 Figure 2. The x-axis is  $\lambda$  (recorded events / number of days in the time series) multiplied by daily  
 891 to 12-week aggregation intervals (days) and the y-axes were the deviations for each of the 27 sites  
 892 in their stochastic time series a,b) means ( $\mu_t^*$ ; note the scale of the y-axis), c,d) standard deviations  
 893 at  $t$ -day ( $\sigma_t^*$ ) divided by the daily standard deviation ( $\sigma_1^*$ ) with blue dashed lines at  $(\lambda n)^{0.5}$  and  
 894  $(\lambda n)^{0.2}$ , and e-g) Pearson correlation coefficients at  $t$ -day divided by daily ( $\rho_t^*/\rho_1^*$ ) with blue  
 895 dashed lines at y-axis = 1. Refer to *Supplemental Materials* (Fig. S1) for larger ranges in y-axis  
 896 values for ( $\rho_t^*/\rho_1^*$ ).

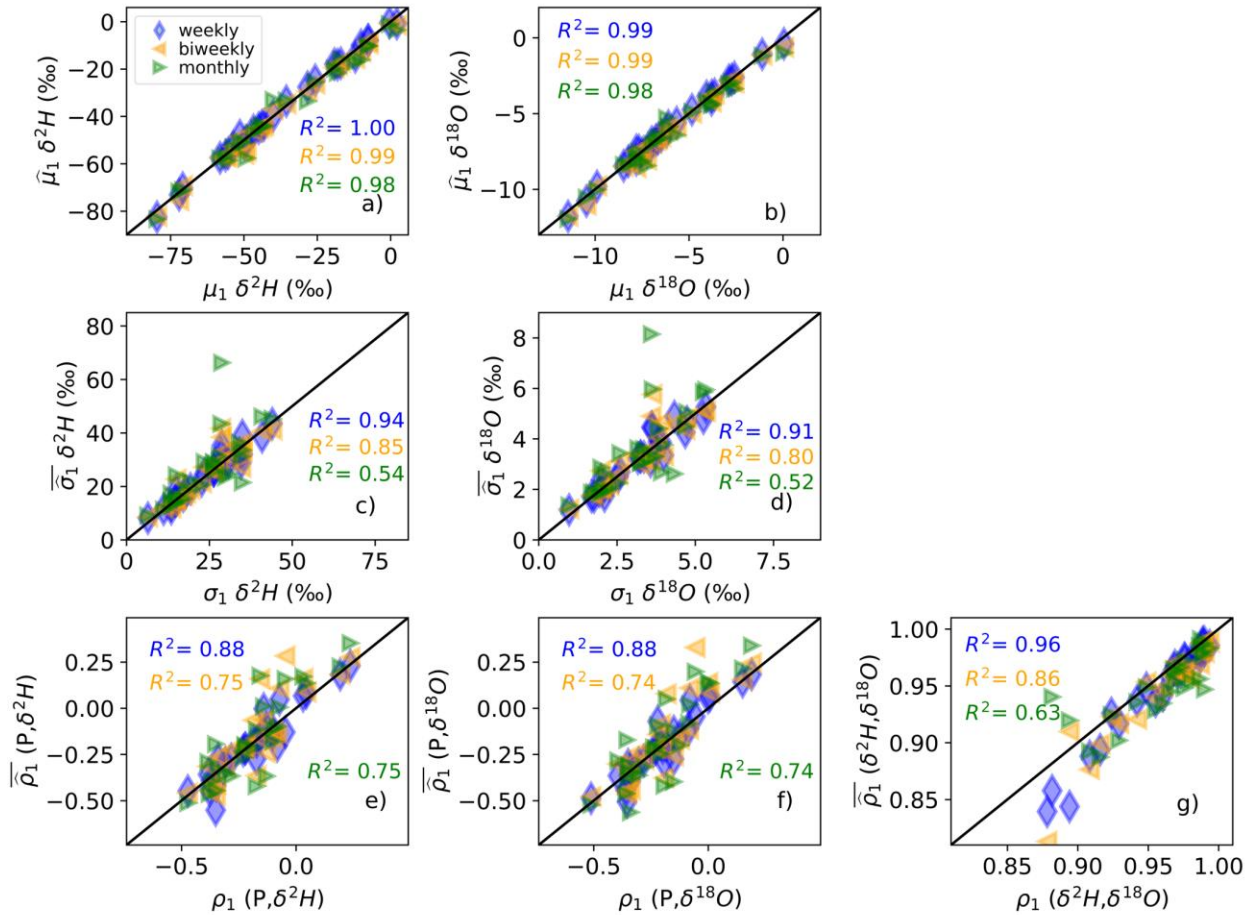
897



898

899 Figure 3. The estimated standard deviations (a,b) and Pearson correlation coefficients (c-e) of  
 900 the stochastic signal from downscaled weekly, biweekly and monthly time series compared to  
 901 the observed daily stochastic statistics. Each data point is one site location and the black lines are  
 902 the 1:1 lines. The means were not shown because they are approximately zero (refer to Figure  
 903 S2.a,b).

904



905

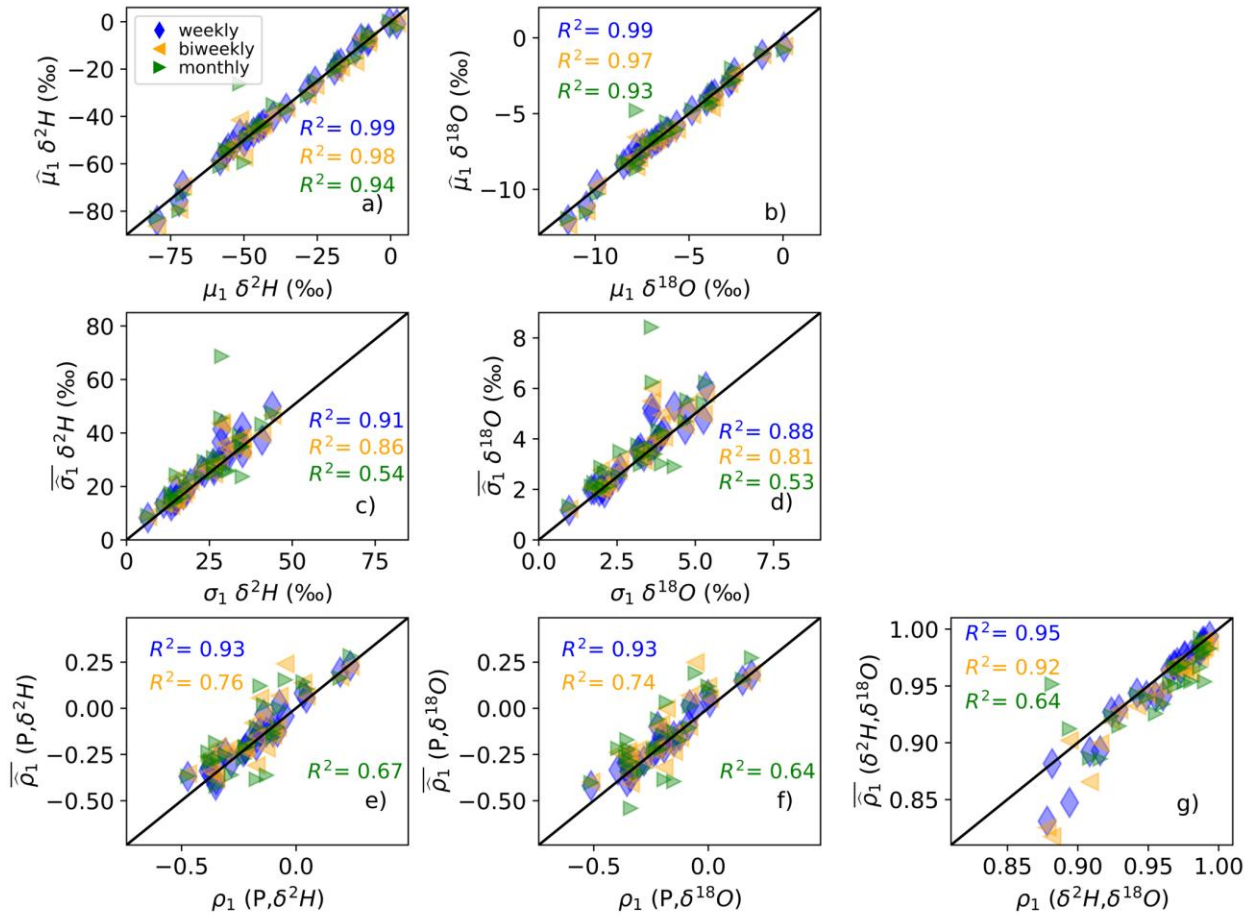
906 Figure 4. The average means (a,b), standard deviations (c,d) and Pearson correlation coefficients

907 (e-g) of the downscaled ensembles from the weekly, biweekly and monthly time series compared

908 to the observed daily site statistics. Each data point is one location and the black lines are the 1:1

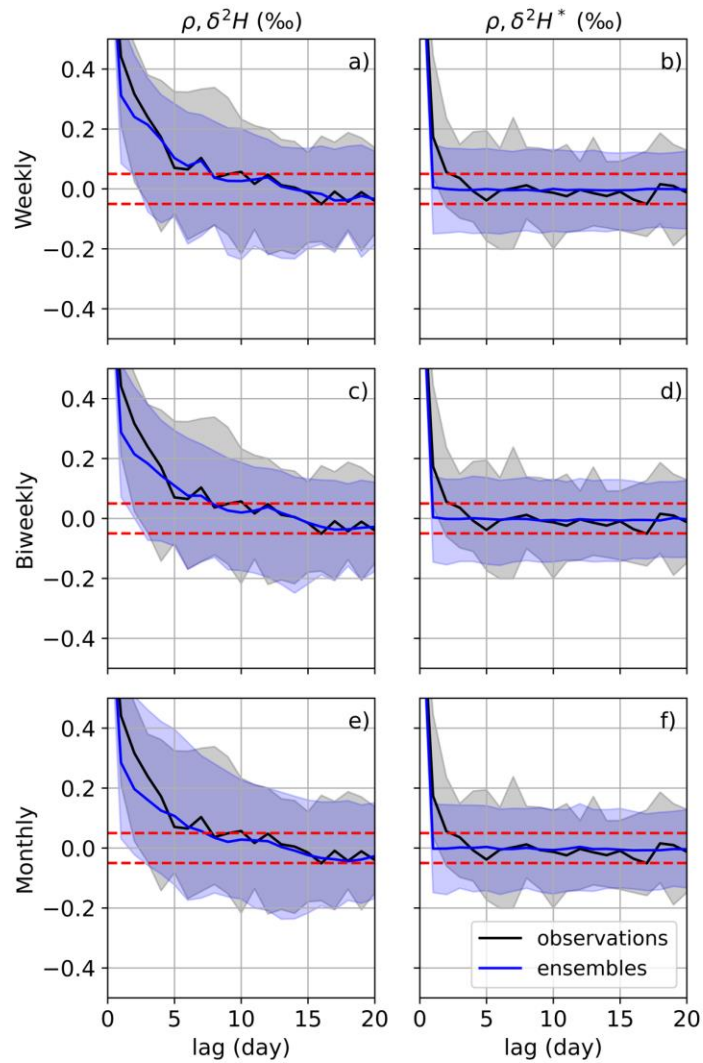
909 lines.

910



911  
 912 Figure 5. The average means (a,b), standard deviations (c,d) and Pearson correlation coefficients  
 913 (e-g) of the residual corrected downscaled ensembles from the weekly, biweekly and monthly  
 914 time series compared to the observed daily site statistics. Each data point is one location and the  
 915 black lines are the 1:1 lines.

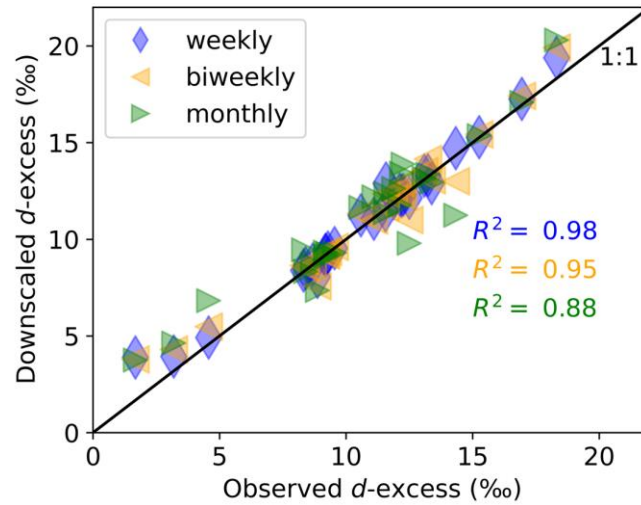
916



917

918 Figure 6. a,c,e) Median autocorrelation of the observed daily  $\delta^2H$  datasets and the daily residual  
 919 corrected ensembles (solid lines). b,d,f) Median autocorrelations of the  $\delta^2H^*$  stochastic signals for  
 920 the observations and the downscaled ensembles. The 5<sup>th</sup> to 95<sup>th</sup> percentiles of the observed and  
 921 ensemble autocorrelations are represented as shaded regions. Horizontal red dashed line indicates  
 922 where  $\rho$  is  $\pm 5\%$ .

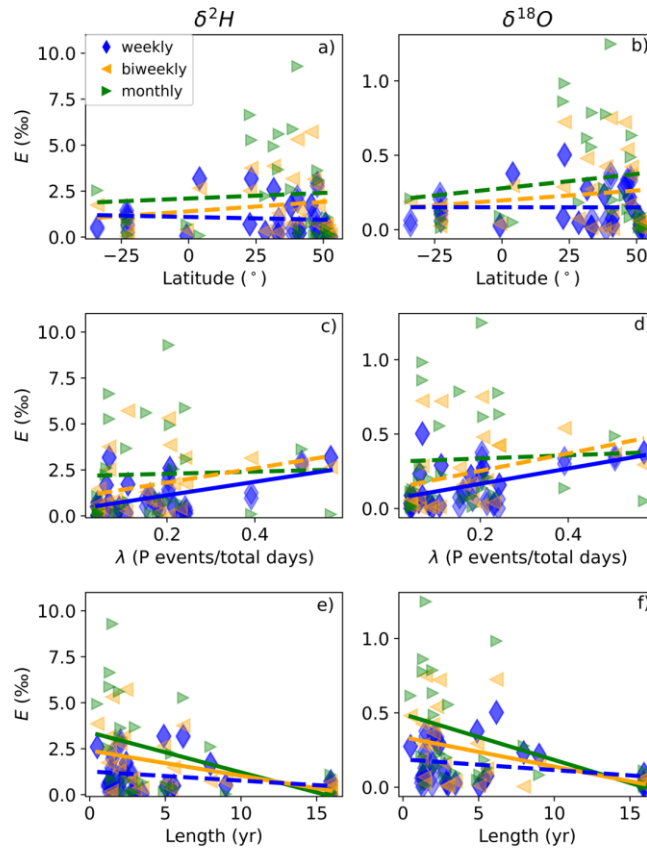
923



924

925 Figure 7. The average  $d$ -excess of the residual corrected downscaled ensemble at each site location  
 926 compared to the average observed  $d$ -excess. Each data point is one site location and the black line  
 927 is the 1:1 line.

928

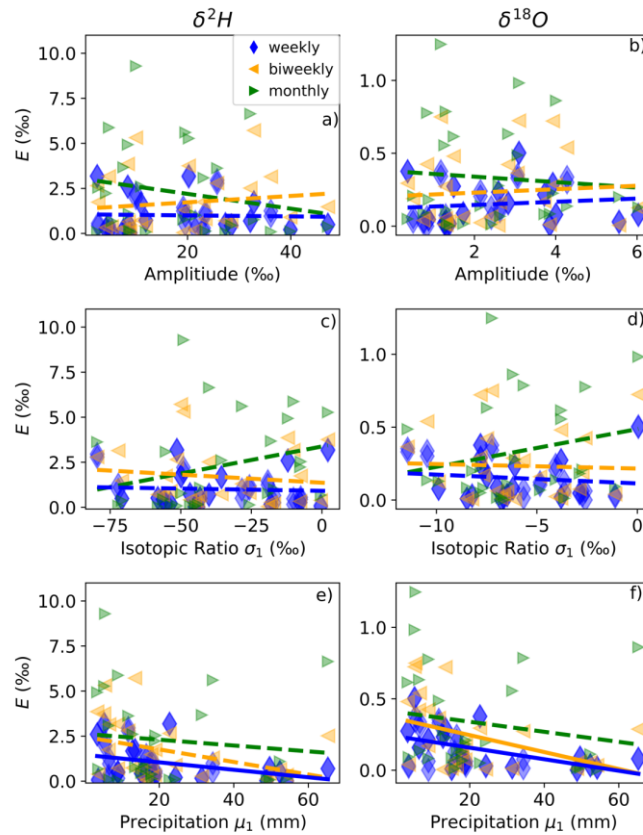


929

930 Figure 8. Absolute error ( $E$ ) of the residual corrected ensemble means compared to various site-  
 931 specific characteristics: a,b) latitude, c,d)  $\lambda$ , and e,f) total length of the time series. Each data  
 932 point is one site location, dashed lines represent p-values  $> 0.05$ , and solid lines represent p-  
 933 values  $< 0.05$ .

934





935

936 Figure 9. Absolute error (E) of the residual corrected ensemble means compared to various site-  
 937 specific characteristics: a,b) the sinusoidal function's estimated amplitude, c,d) standard deviation  
 938 of each isotope ratio and e,f) average daily precipitation. Each data point is one site location,  
 939 dashed lines represent p-values > 0.05, and solid lines represent p-values < 0.05.